VNIR/SWIR Laboratory Imaging Spectroscopy for Wall-to-Wall Mapping of Elemental Concentrations in Soil Cores

SIMON SCHREINER, HENNING BUDDENBAUM, CHRISTOPH EMMERLING, Trier & MARKUS STEFFENS, Freising

Summary: Visible/near infrared (VNIR, 400 nm to 1000 nm wavelength) and shortwave infrared (SWIR, 1000 nm to 2500 nm wavelength) laboratory imaging spectroscopy with spatial resolutions of 63 µm and 250 µm, respectively, was used for mapping contents of C, N, Fe, Al, and Ca in soil profiles. Four soil cores of 30 cm to 50 cm length were collected at a Regosol and a Cambisol site and scanned hyperspectrally after drying. Small samples (ROI; Regions of Interest) were taken from the cores and analysed chemically as references for regression analyses. Partial least-squares regression (PLSR) and multivariate adaptive regression splines (MARS) models between spectral information and elemental contents of reference samples were established for VNIR and SWIR data separately and for the combined datasets. The regression models were applied to the hyperspectral image data to create spatially explicit maps of elemental contents for the soil profiles. PLSR yielded slightly better regression accuracies than MARS, and PLSR maps were more plausible in visual inspection. The optimal spectral range for elemental mapping was inconsistent, but in most cases the addition of SWIR data to VNIR data resulted in improvements of the elemental content estimations.

Zusammenfassung: *Abbildende Laborspektroskopie im VNIR/SWIR-Bereich zur flächendeckenden Kartierung von Elementkonzentrationen in Bodenprofilen.* Hyperspektrale Laboraufnahmen in den Wellenlängenbereichen Sichtbar/Nahinfrarot (VNIR, 400 nm bis 1000 nm Wellenlänge) und Kurzwelleninfrarot (SWIR, 1000 nm bis 2500 nm) mit räumlichen Auflösungen von 63 µm und 250 µm wurden verwendet, um die räumlichen Verteilungen von C, N, Fe, Al und Ca in Bodenprofilen zu kartieren. Vier Bodenkerne mit 30 cm bis 50 cm Länge wurden an einem Cambisol- und einem Regosol-Standort entnommen und im Labor hyperspektral abgetastet. Kleine Proben wurden aus den Profilen entnommen und als Referenz für die nachfolgenden Regressionsanalysen chemisch analysiert. Regressionsmodelle wurden mittels Partial Least-Squares Regression (PLSR) und Multivariate Adaptive Regression Splines (MARS) zwischen Spektralinformationen und Elementkonzentrationen der Referenzproben aufgestellt, separat für VNIR- und SWIR-Daten und für die kombinierten Datensätze. Die Regressionsmodelle wurden auf die Bilddatensätze angewendet, um Karten der Elementkonzentrationen in den Bodenprofilen zu erzeugen. Die Regressionsgenauigkeiten von PLSR waren leicht höher als die von MARS, und die PLSR-Karten gaben einen visuell plausibleren Eindruck. Der optimale Spektralbereich zur Kartierung der verschiedenen Elemente war uneinheitlich. Aber meistens brachte die Berücksichtigung der SWIR-Daten eine Verbesserung gegenüber den VNIR-Daten alleine.

1 Introduction

Visible/near infrared (VNIR, 400 nm to 1000 nm wavelength) and shortwave infrared (SWIR, 1000 nm to 2500 nm wavelength) dif-

fuse reflectance spectroscopy has proven to be useful for many soil scientific topics. Reflectance spectroscopy has been used in many studies for the determination of soil properties like mineral composition (VISCARRA ROS-

SEL et al. 2009), texture (STENBERG 2010), biological properties (HEINZE et al. 2013), soil salinity (FARIFTEH et al. 2008), or chemical composition (VOHLAND et al. 2009). The papers by VISCARRA ROSSEL et al. (2006), BEN-DOR et al. (2009), STENBERG (2010) and HARTEMINK & MINASNY (2014), among many others, give an overview on techniques and results of reflectance spectroscopy in soil science.

In most studies, reflectance spectroscopy was either used on samples from selected points (field and laboratory spectroscopy), or on the soil surface (airborne and spaceborne imaging spectroscopy). Recently, JUNG et al. (2015) introduced a hyperspectral snapshot camera for proximal soil sensing.

The horizontal variability of soil surfaces is usually slow and gradual, but variability in the third dimension, depth, is much higher (VISCARRA ROSSEL et al. 2015). Information on vertical variability is needed, among others, for interpretations of soil formation processes, characterizations of the soil horizons and the detection of small scale soil processes like bioturbation. The technique of laboratory imaging spectroscopy of soil cores using a hyperspectral line scanner was introduced by BUDDENBAUM & STEFFENS (2011) for spectroscopic analysis of undisturbed soil profiles with a very high spatial resolution. Applying this proximal sensing technique for the creation of elemental maps by using support vector regression and PLSR was presented by BUDDENBAUM & STEFFENS (2012b). Effects of spectral pre-treatments on elemental regressions using VNIR laboratory imaging spectroscopy were studied by BUDDENBAUM & STEFFENS (2012a). The approach was extended to include horizon classification and geostatistical characterization of a soil profile (STEFFENS & BUDDENBAUM 2013), and soil organic matter quality (STEFFENS et al. 2014). While these studies used only VNIR spectroscopy, SWIR cameras are now available with a comparable spatial resolution for laboratory use. Since many mineralogic absorption features are situated in the SWIR spectral region, an improved elemental mapping could be expected from adding SWIR information.

For the present study, soil cores were sampled from a Cambisol under Norway spruce and a Regosol under European beech stand close to Trier, Germany. Hyperspectral images of the cores were recorded using a VNIR camera and a SWIR camera. The content of C, N, Fe, Al, and Ca was analysed on reference samples with standard laboratory techniques. Spectra of the reference samples were used to establish regression models (PLS regression and MARS). These models were used to create maps of the elemental concentrations in the soil cores. Main research objectives were (1) to compare the regression techniques for elemental mapping of various elements, (2) to compare the predictive capacity of the VNIR and SWIR spectral range, and (3) to compare the two sampling sites in terms of elemental contents and distributions.

2 Material and Methods

2.1 *Study Site and Soil Sampling*

The sampling was carried out approximately 12 km northeast of Trier (Rhineland Palatinate, 49.84°N, 6.71°E). Two differing soil types were sampled. The first soil type was classified as an albic Cambisol under a Norway spruce monoculture, the second soil was a colluvic gleyic Regosol (WRB 2014) close to a creek under a European beech monoculture. Both soils derived from Triassic Sandstone (Buntsandstein). The study site is characterized by temperate, oceanic climate conditions with a mean annual temperature of 9.1 °C and a mean annual precipitation of 780 mm.

The soil profiles were sampled with custom-made stainless steel boxes. Two boxes with $100 \times 100 \times 300$ mm³ size and two boxes with $100 \times 100 \times 500$ mm³ were available. They were designed to sample undisturbed sections of soil profiles. After digging a hole and removing the litter layer, the steel boxes were gently hammered horizontally into the soil and subsequently excavated. In the lab, the soil cores were dried in the steel boxes at 35 °C for one week. Two profiles of different depths were sampled for each soil type, one of 30 cm and the other of 50 cm depth. The two profiles of albic Cambisol are subsequently indicated as Cambisol30 and Cambisol50, and the colluvic gleyic Regosol profiles as Regosol30 and Regosol50.

2.2 *Imaging Setup*

After smoothing the surface of the soil profile with a long knife, the images were recorded using a HySpex VNIR-1600 and a HySpex SWIR-320m-e hyperspectral camera (Norsk Elektro Optikk, Skedsmokorset, Norway) at the Department of Environmental Remote Sensing and Geoinformatics at the University of Trier (BUDDENBAUM & HILL 2015, BUDDENBAUM et al. 2015). The cameras were equipped with a 30 cm focal lens and set up in a laboratory frame with a translation stage under the camera. The translation stage moves the object in along-track direction, while the camera, a push-broom scanner, records image lines across track. The speed of the translation stage is adapted so that square pixels result.

For the VNIR images two tungsten halogen light sources illuminate the currently scanned line from about 35 cm distance and at an angle of about 45° in front of and behind the camera to minimize shadows on the soil surface. The VNIR-1600 camera records 1600 pixels across track with a field of view of 17°. The pixel instantaneous field of view is 0.18 mrad across track and 0.36 mrad along track. The area recorded from the 30 cm distance is 10 cm wide, so that the size of a single pixel amounts to about 63 μm. A 30 cm long soil profile consists of approximately 4800 image lines, a 50 cm profile of 8000 image lines. About 200 additional image lines containing a certified reflectance standard white reference panel of known reflectivity (Spectralon, Labspere Inc., North Sutton, NH, USA) were scanned with each sample, so radiance could be transformed to reflectance. 160 spectral bands were recorded in the spectral range of 414 nm to 1000 nm with a spectral sampling interval of 3.7 nm. The data was recorded in 12 bit radiometric resolution.

The laboratory frame can only hold one camera at a time, so the SWIR images were recorded after the VNIR datasets. Because the light source used for VNIR imaging only covers the spectral range up to 1700 nm, a stabilized tungsten halogen lamp (50 W) was used for illumination. The SWIR-320m-e camera records 256 spectral bands in the spectral range of 1000 nm to 2500 nm with a field of view of 13.5°. 320 pixels are acquired across track; a single pixel is about 250 μm wide. The 30 cm profiles consist of approximately 1200 lines, the 50 cm profiles of 2000 lines. The SWIR images were also recorded with a Spectralon white reference panel which covered about 50 lines.

2.3 *Image Pre-Processing*

Because the illumination was not perfectly uniform, the object reflectance ρ_{obj} was calculated for each image line (along track) separately following (1):

$$\rho_{obj} = \frac{L_{obj}}{L_{ref}} \cdot \rho_{ref} \qquad (1)$$

where L_{obj} is the measured radiance from the object in camera units, L_{ref} is the measured radiance from the white reference and ρ_{ref} is the known reflectance of the white reference panel (PEDDLE et al. 2001).

Different pre-processing steps have been applied by several authors, e.g. BEN-DOR et al. (1997), BUDDENBAUM & STEFFENS (2012a), UDELHOVEN et al. (2003), and VISCARRA ROSSEL & WEBSTER (2011), but in combination with PLSR, these transformations were not able to increase regression accuracy significantly. To improve the signal-to-noise ratio, we applied spectral resampling, a bisection of the spatial resolution of the VNIR images, and continuum removal (CR). Spectral resampling implies an increase of the spectral sampling interval and the full width at half maximum from 3.7 nm to 7.3 nm in the VNIR range and from 7 nm to 15 nm in the SWIR range. With this transformation, neighbouring spectral bands were averaged, and the number of bands was reduced from 160 to 78 bands (VNIR) and from 256 to 100 bands (SWIR). The spatial resolution of the VNIR images was bisected by averaging 2×2 pixels to one resulting pixel. CR is a tool to amplify reflective features and especially to amplify absorption bands in a spectrum. This is done by fitting a convex hull to the spectrum and dividing the reflectance values for each wavelength by the reflectance level of the continuum line (convex hull) at the corresponding wavelength (KOKALY & CLARK 1999). This pre-processing returns a CR value of 1 to all

parts of the spectrum that lie on the convex hull, i.e. wavelength regions that are not in an absorption band, and values between 0 and 1 to regions inside absorption bands. So CR accentuates the absorption bands in the spectra while minimizing brightness differences. The recorded images mostly have a high quality, but despite efforts to reduce noise, some noise is still present, especially in the SWIR range. The noise is most obvious in vertical stripes on the images.

To obtain spectra from 400 nm to 2500 nm for each pixel, an image-to-image geometric correction was applied. Ground control points (GCP) were identified in the images and used for warping the SWIR image to the VNIR image's geometry using a rubber sheeting (local triangulation) approach.

Homogeneous regions of interest (ROIs) of about 2 cm² area were regularly distributed over the soil profiles (18 ROIs on each of the 50 cm profiles and 12 ROIs on each of the 30 cm profiles) and mean spectra of these ROIs were extracted.

2.4 Chemical Analysis

The ROIs were visually identified in the soil core and samples of about 2 cm² and about 1 cm depth were taken for chemical laboratory analysis. After thoroughly sieving to < 2 mm and grinding, samples were oven-dried at 105 °C. Total organic carbon (TOC) and total nitro-

gen (TN) concentrations were determined in duplicate by dry combustion at 1100 °C by a EuroEA elemental analyzer (Hekatech GmbH, Wegberg, Germany) in carbonate-free samples. Total amounts of aluminum (Al), iron (Fe) and calcium (Ca) were extracted with 3 ml concentrated HNO_3 and 1 ml H_2O_2 (suprapur) in 0.1 g – 0.2 g dry mass using high pressure bombs (Berghof, Eningen, Germany) (UDELHOVEN et al. 2003). Element concentrations were measured with an atomic absorption spectrometer (Varian AA 240 FS and AA 240Z/GTA 120, Palo Alto, CA, U.S.A.).

2.5 Elemental Mapping

We compared two statistical methods for establishing regression models between elemental concentrations and reflective properties: Partial least-square regression (PLSR), and Multivariate adaptive regression splines (MARS). The regression analyses were carried out in MATLAB (Version R2012, Mathworks, Natick, MA, USA). All models were established on reflectance and chemical data from both soils and all horizons combined.

Partial least-square regression (PLSR) after WOLD et al. (2001) is a widely used approach for quantitative analysis in chemometrics and hyperspectral remote sensing (FARIFTEH et al. 2007, STEFFENS & BUDDENBAUM 2013, VISCARRA ROSSEL & BEHRENS 2010, VOHLAND & EMMERLING 2011). PLSR is closely related to
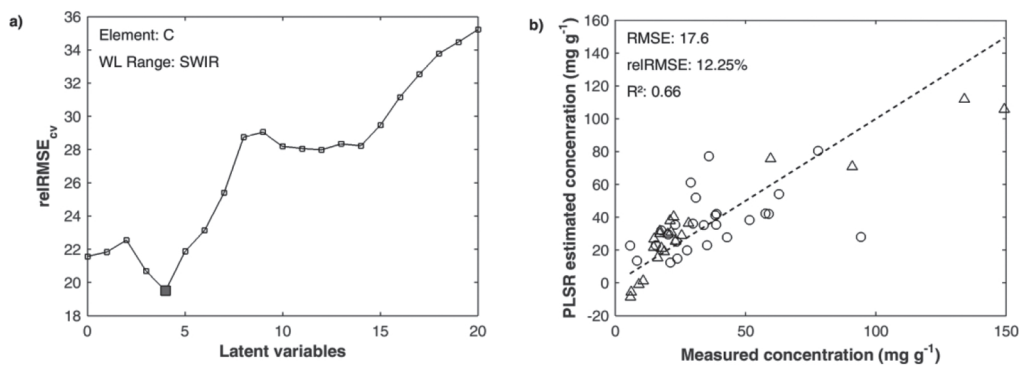

Fig. 1: PLS regression of C using the SWIR wavelength range: a) relative cross-validated RMSE as a function of the number of latent variables, best model at 4 latent variables is marked; b) measured versus C contents estimated using the model with 4 latent variables (Regosol: circles, Cambisol: triangles), and the 1:1 line.

principal components regression (PCR) and combines features from PCR and multiple regression (MARABEL & ALVAREZ-TABOADA 2013, WOLD et al. 2001a). PLS regression projects the data (chemical concentrations and reflective properties with a high number of correlated variables) into a lower dimensional space, formed by a set of orthogonal latent variables, by a simultaneous decomposition of X (spectral matrix) and Y (chemical matrix) that maximizes the covariance between X and Y (VOHLAND & EMMERLING 2011, WOLD et al. 2001b). A large number of measured collinear spectral variables is reduced to a few non-correlated latent variables (MARABEL & ALVAREZ-TABOADA 2013), which also implements a reduction of the data volume and the calculation time. The method is well suited for the calibration of a small number of samples with experimental noise in both chemical and spectral data (ATZBERGER et al. 2010), even if the number of observations is smaller than the number of wavelengths (BEN-DOR et al. 2008).

To find the optimum number of latent variables, we calculated PLSR models with up to 20 latent variables on the ROI spectra for each analyzed element, separately for all VNIR-, SWIR-, and full range images. We applied a five-fold cross validation and a 100-fold Monte Carlo repetitions to each model to avoid overfitting (SCHLERF et al. 2010) and calculated the cross-validated relative root-mean-square error (relRMSEcv) for each model.

Fig. 1a illustrates the relationship between number of latent variables and relRMSEcv. The model with lowest relRMSEcv was selected. With this optimal number of latent variables, a new PLSR is calculated and applied on the hyperspectral images to create maps of the distribution of the element in question. Resulting concentrations for C using the SWIR wavelength range and four latent variables compared to the laboratory measured concentrations are shown in Fig. 1b. No further calibration/validation scheme was applied, because plausible maps resulted from this strategy. Fig. 2 shows the regression coefficients (PLS weights) for each element and each wavelength range. The regression coefficients have been normalized for displaying them in the figure by subtracting their mean and dividing the result by their standard deviation (z-transformation). The plots show the important wavelength regions for estimating the elemental concentrations.

Multivariate adaptive regression splines (MARS) after FRIEDMAN (1991) is a non-parametric generalization of recursive partitioning
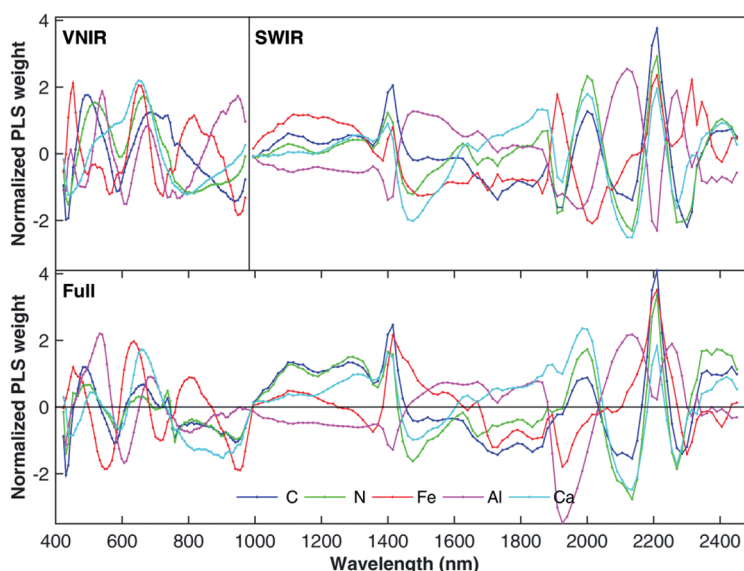

Fig. 2: Normalized weights of the input bands in the three PLS regressions (VNIR, SWIR, and full wavelength range).

regression approaches such as classification and regression trees (CART) (VISCARRA ROSSEL & BEHRENS 2010). It makes no assumption about the underlying functional relationship between the dependent and independent variables. NAWAR et al. (2015) found that MARS was better suited for the visible and near-infrared reflectance spectroscopy estimation of soil salinity than PLSR.

The MARS models were evaluated using a five-fold cross validation and 100 Monte Carlo repetitions. Elemental maps were then calculated by applying the models on a pixel-by-pixel basis on the hyperspectral images.

Even though the profiles were illuminated from two directions, the formation of shadow because of strong surface roughness was unavoidable. Parts of the profiles with high carbon and nitrogen or iron-concentrations are dark coloured. The spectral signatures of these parts are similar to the shadow signatures, which results in false values. To correct this, shadows had to be determined and the profiles shadow masked. Shadows were detected using a principal component analysis followed by an unsupervised classification. One of the resulting classes corresponded well with shadowed areas in a visual inspection. After building a shadow mask for each profile, this mask was applied on the respective image (STEFFENS & BUDDENBAUM 2013).

3 Results and Discussion

3.1 *Elemental Concentrations*

The high variance of carbon and nitrogen content in both soils are shown in Tabs. 1 and 2. Typically, in both soils a vertical element gradient was clearly developed with high organic matter content in the topsoil and decreasing amounts with increasing depth. The thickness of the humus-rich A-horizon ranged from 6 cm to 10 cm depending on the respective soil profile. Mean concentrations of TOC in the topsoil reached more than 200 mg g^{-1}, whereas in the subsoil it was about 20 mg g^{-1} – 30 mg g^{-1}. Nitrogen showed the same trend, with amounts in a range from 0.2 mg g^{-1} – 16 mg g^{-1}. Maximum C contents of 291 mg g^{-1} (Cambisol) or 339 mg g^{-1} (Regosol) might be attributed to residues of the litter layers, which have not been involved in the soil sampling schedule. Both soils derived from siliceous bedrocks (Sandstones) and thus, as expected, soil pH in these soils varied between 4.5 and 5.0, which is equivalent to the silicate buffer capacity of soil. As a consequence, soils were carbonate-free and thus, amounts of total carbon in soil were equivalent to total organic carbon.

Amounts of Fe, Al, and Ca in both soils showed a different element distribution in the soil profile compared to carbon and nitrogen. Although there was a remarkable variability in the amounts of Fe and Al, the differences in both elements between the top soils and the sub-soils of both investigated soil profiles remained small. The differences in the element distribution of Fe and Al between both soils were also quite small and in a typical range of those soils. Similarly, Ca was concentrated in the top soil and amounts of Ca in the subsoil were in both soils roughly at the detection limit. This result can also be attributed to the parent material and forestal land-use of both soils.

Tab. 1: Descriptive statistics of the Regosol including minimum (Min), maximum (Max), mean of concentrations of all five elements. Negative values result from detection limits in the analysis and were treated as zero in further analyses.

Colluvic Gleyic Regosol					
	C (mg g^{-1})	**N (mg g^{-1})**	**Fe (mg g^{-1})**	**Al (mg g^{-1})**	**Ca (mg g^{-1})**
Min	5.7	0.2	0.44	3.26	-0.42
Max	338.8	16.1	4.66	17.06	1.77
Mean Topsoil	270.8	13.4	3.42	3.63	1.26
Mean Subsoil	36.5	1.7	1.36	9.35	-0.10
Mean full profile	71.2	3.5	1.66	8.50	0.10

Tab. 2: Descriptive statistics of the albic Cambisol containing minimum (Min), maximum (Max), mean of concentrations of all five elements in their specific units. Negative value results from detection limits in the analysis and was treated as zero in further analyses.

	C (mg g⁻¹)	N (mg g⁻¹)	Fe (mg g⁻¹)	Al (mg g⁻¹)	Ca (mg g⁻¹)
Albic Cambisol					
Min	5.9	0.2	1.70	4.11	-0.16
Max	290.7	10.4	5.54	15.60	2.83
Mean Topsoil	199.7	7.3	3.05	5.69	1.57
Mean Subsoil	24.5	0.8	3.05	8.09	-0.02
Mean full profile	50.5	1.8	3.05	7.73	0.22

Tab. 3: Intercorrelations of the elemental concentrations.

	C	N	Fe	Al	Ca
C	1				
N	0.979	1			
Fe	0.286	0.259	1		
Al	-0.318	-0.324	-0.027	1	
Ca	0.897	0.831	0.255	-0.329	1

Tab. 4: Statistical comparison of the PLSR models. For each element and wavelength range statistically best result (relRMSE and R^2) and corresponding number of latent variables (LV) is listed. Data for the two soils are combined.

	VNIR			SWIR			Full		
	relRMSE / %	R²	#LV	relRMSE / %	R²	#LV	relRMSE / %	R²	#LV
C	15.32	0.468	4	12.25	0.660	4	**10.13**	**0.767**	7
N	12.54	0.601	3	9.44	0.774	4	**8.16**	**0.831**	7
Fe	9.78	0.818	7	17.55	0.415	4	**9.58**	**0.826**	7
Al	21.71	0.340	5	21.02	0.381	4	**19.42**	**0.472**	5
Ca	9.68	0.767	3	7.82	0.848	4	**6.34**	**0.900**	6

Tab. 5: Statistical comparison of the MARS models. Best results are displayed in bold. Data for the two soils are combined.

	VNIR		SWIR		Full	
	relRMSE	R²	relRMSE	R²	relRMSE	R²
C	25.27	0.250	30.86	0.215	**24.62**	**0.300**
N	22.08	0.209	24.42	0.285	**19.77**	**0.353**
Fe	**18.84**	**0.451**	30.91	0.130	22.45	0.339
Al	**27.91**	**0.186**	33.38	0.101	32.59	0.126
Ca	**12.50**	**0.682**	16.04	0.629	14.55	0.632

Intercorrelations between the elemental concentrations are listed in Tab. 3. C and N are very highly correlated with each other and highly correlated with Ca. Fe and Al show no correlation with each other and low correlations with the other elements.

3.2 *Regression Models of Elemental Concentrations*

For each element, multiple concentrations maps (derived from different wavelengths ranges: VNIR, SWIR, and full range) were calculated combining data from the two soils. relRMSE and R^2 of the statistically best results are shown for each element and each wavelength range in Tabs. 4 and 5 for PLSR and MARS, respectively.

Using PLSR, most elements are estimated best with the full wavelength range. Surprisingly, C estimations using SWIR data are better than VNIR-based estimations, although it is well known that a high organic carbon amount colours the soil dark in the visible spectral region (Stoner & Baumgardner 1981).

Tab. 5 gives an overview of the statistical results using MARS. In the visual comparison, almost all MARS maps were inferior to the PLSR maps, and R^2 and relRMSE values of the MARS models are lower than the PLSR values, which is in contrast to the results of Nawar et al. (2014). Best statistical values for the organic matter (C and N) are in the full wavelength range. Best models for Fe, Al, and Ca are in the VNIR wavelength range, which is plausible for iron because of the broad absorption bands between 0.6 µm and 1.5 µm (Mulders 1987). Fig. 3 shows scatter plots of MARS estimations of C for the three wavelength regions. The scatter plot in the VNIR wavelength range shows a narrow distribution of most samples on the 1:1 line for the lower values, but some strong outliers in the range above 50 mg g^{-1} (Fig. 3a). The distribution in the SWIR wavelength range is generally similar, with one outlier even far in the negative range (Fig. 3b). R^2 in the SWIR is lowest and RMSE is highest. In the full wavelength range the scatter is still high, but outliers are less extreme and thus the highest R^2 and lowest

RMSE values are achieved (Fig. 3c). The high amount of image noise in the resulting maps and the fact that in most cases the full wavelength range does not lead to the highest accuracies hint to some sensitivity to noise and overfitting in MARS.

Selected elemental maps showing the strengths and weaknesses of the statistical results are discussed. Fig. 4 displays PLSR-derived maps of the five elements for the profile Cambisol50. Each map covers a profile area of 10 cm width and 50 cm depth. All maps reflect the spatial distribution well and have plausible ranges of values. C mainly accumulates in the top-horizon, but also in the subsoil, isolated organic residues are recognizable, e.g. caused by roots. Due to the very high correlation between C and N contents, the N map has similar distributions; organic residues in the subsoil region are even better recognizable in the nitrogen map than in the C map. The Fe content is relatively homogenous throughout the profile because of the iron-rich parent material. Al shows a pattern similar to Fe, but the maximum is in a lower region of the profile.

The Ca profile in Fig. 4 has to be discussed carefully, because concentrations in the subsoils (of both soils) were sometimes under the detection limit. There are some patches of Ca concentrations which might have remained from previous liming events.

Fig. 5 shows a comparison of C in the Cambisol30 profiles created using the three wavelength ranges and PLS regression. In the VNIR profile, accumulations of C are visible in the humus-rich top soil and in organic residues (roots) in the subsoil regions. The SWIR profile accentuates regions of high C content more strongly. The full range data leads to the most contrast-rich map of C but also shows the most image noise.

Some maps created with MARS can be seen in Fig. 6. While C, N, and Al are mapped in acceptable quality, the maps of Fe and Ca are quite noisy. According to the reference measurements, C and N concentrations are highest in the topsoil, but MARS is unable to capture that.
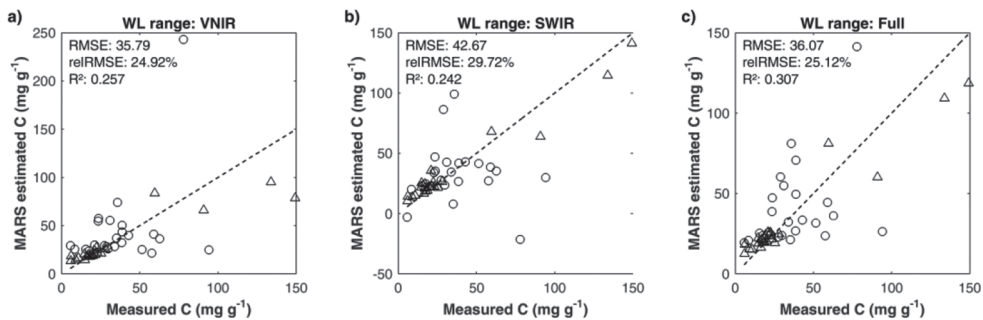
Fig. 3: Measured against MARS estimated C concentrations (with 1:1 lines) using different wavelength ranges (Regosol: circles, Cambisol: triangles).
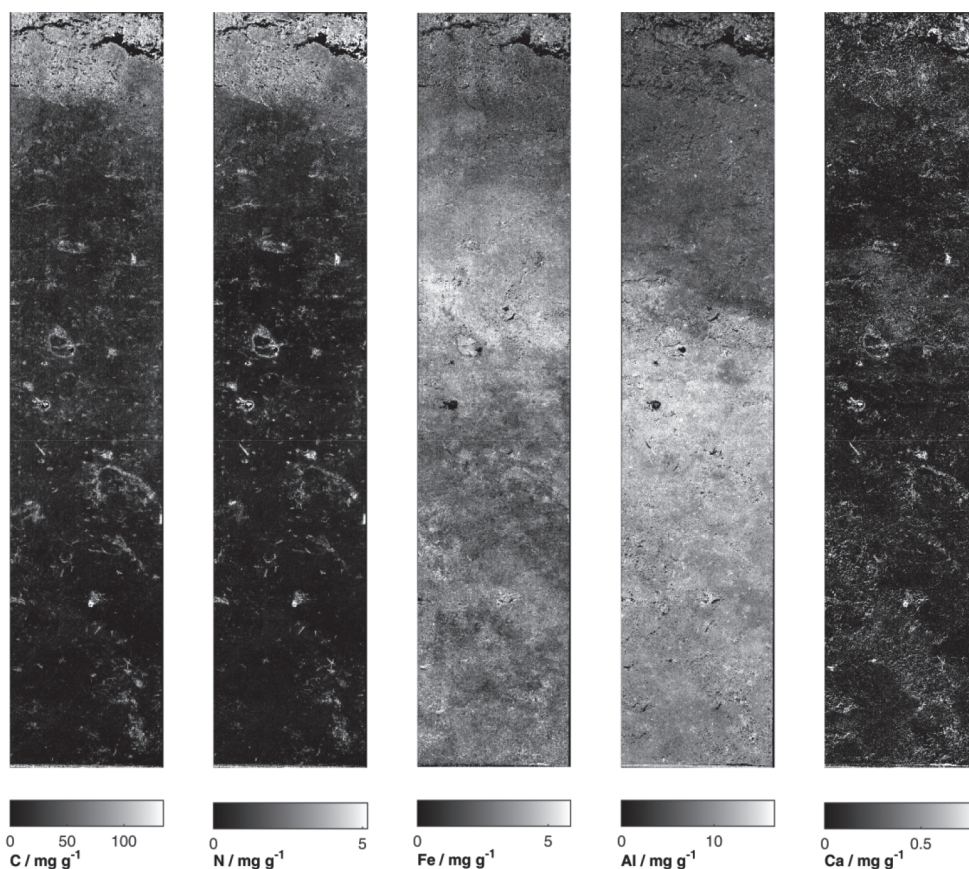

Fig. 4: Maps of the 5 elements in the 50 cm long Cambisol profile according to PLS regression using the full wavelength range. The grey levels are stretched linearly from 0 (black) to the 98th percentile of values present in each map (white).
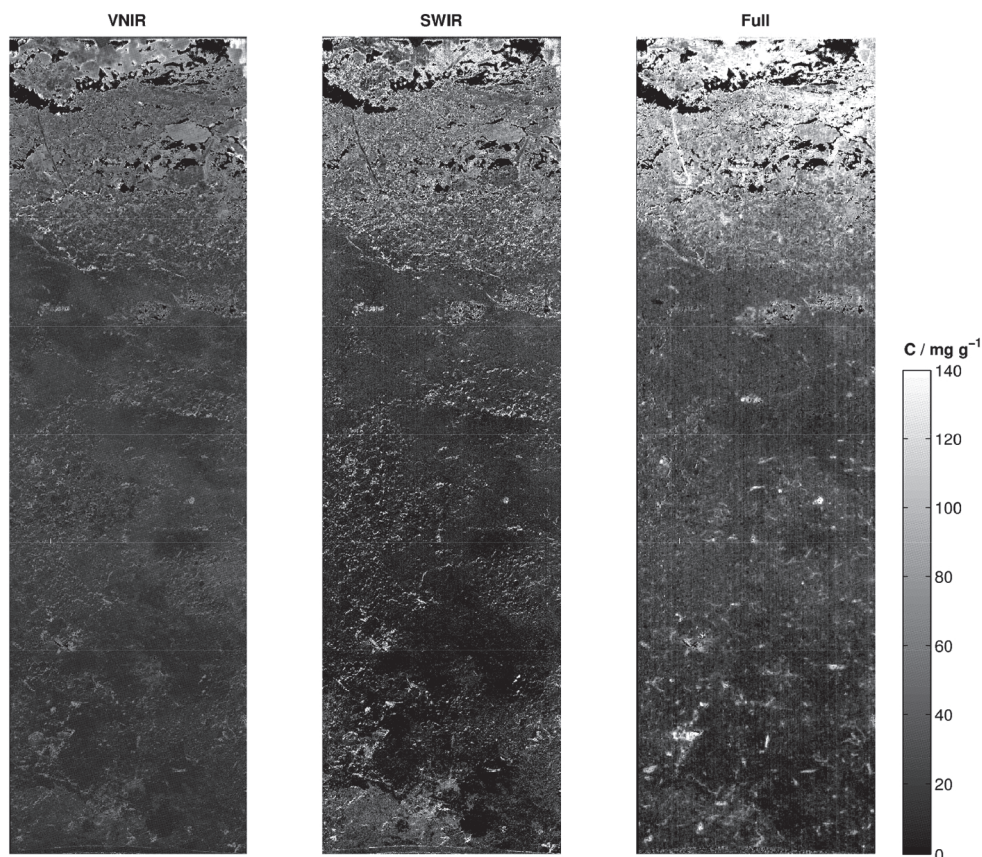
Fig. 5: Comparison of PLSR C maps of the Cambisol30 profile created with three different wavelength ranges. The grey levels are stretched linearly from 0 (black) to the 98th percentile of value of the full range map (white).

4 Conclusions

In this study, elemental concentrations in soil profiles were mapped using laboratory imaging spectroscopy. We compared three spectral ranges, i.e. VNIR, SWIR, and full range images, and two regression methods, i.e. MARS and PLSR.

PLSR was better suited for elemental mapping, both in terms of statistical measures and in visual quality of the resulting maps. This study confirms PLSR as a powerful regression tool that makes use of all input bands and serves well in identifying important spectral bands representing specific elemental concentrations in natural soil profiles. PLSR is less affected by image noise, while the MARS maps emphasize the noise that is present in the image data.

While previous studies used exclusively the VNIR camera, the additional information retrieved using a SWIR camera was tested in this study. The elemental maps using only the HySpex SWIR-320m-e module were not always reasonable, but regressions including VNIR and SWIR wavelengths in combination lead to improved statistical results.

The resulting maps show elemental distribution in a very high spatial resolution and can be used for further analyses of the soil cores and their horizons. Consequently, laboratory imaging spectroscopy of soil profiles in the
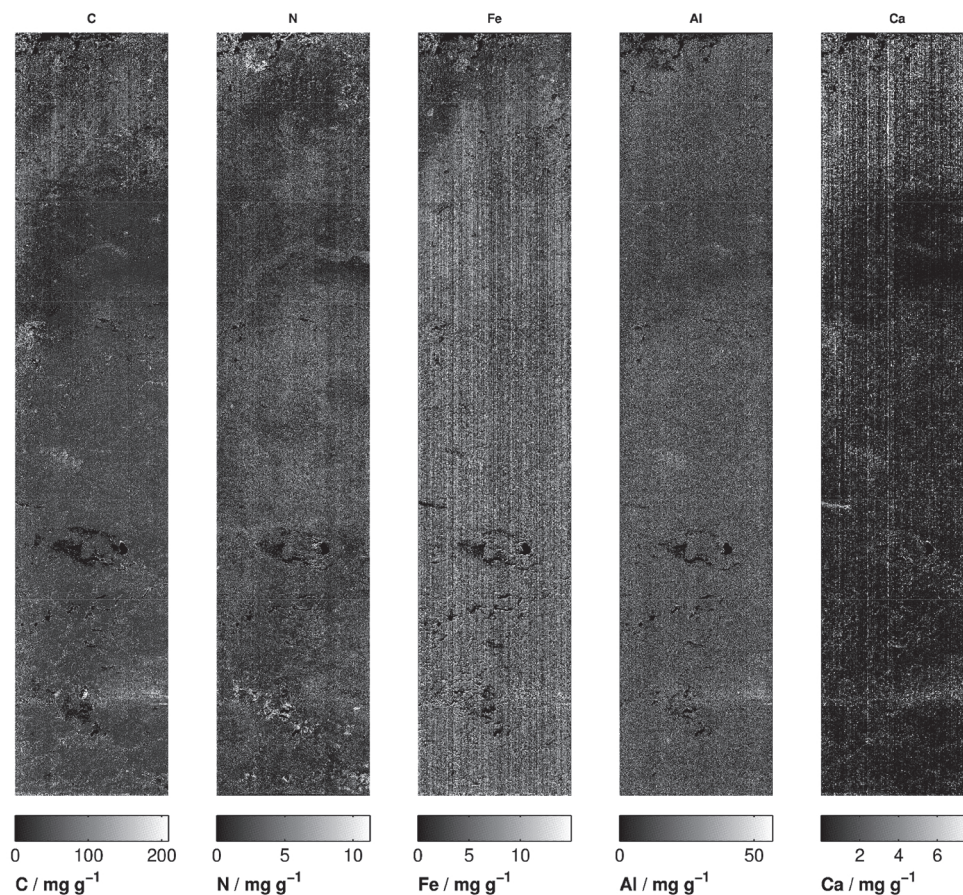
Fig. 6: Maps of the 5 elements in the 50 cm long Regosol profile according to MARS regression. The grey levels are stretched linearly from 0 (black) to the 98th percentile of values present in each map (white).

VNIR/SWIR range has proved to be a promising and reliable novel technique for various soil scientific topics.

References

ATZBERGER, C., GUÉRIF, M., BARET, F. & WERNER, W., 2010: Comparative analysis of three chemometric techniques for the spectroradiometric assessment of canopy chlorophyll content in winter wheat. – Computers and Electronics in Agriculture **73** (2): 165–173.

BEN-DOR, E., INBAR, Y. & CHEN, Y., 1997: The reflectance spectra of organic matter in the visible near-infrared and short wave infrared region (400 nm – 2500 nm) during a controlled decomposition process. – Remote Sensing of Environment **61** (1): 1–15.

BEN-DOR, E., HELLER, D. & CHUDNOVSKY, A., 2008: A Novel Method of Classifying Soil Profiles in the Field using Optical Means. – Soil Science Society of America Journal **72** (4): 1113–1123.

BEN-DOR, E., CHABRILLAT, S., DEMATTÊ, J.A.M., TAYLOR, G.R., HILL, J., WHITING, M.L. & SOMMER, S., 2009: Using Imaging Spectroscopy to study soil properties. – Remote Sensing of Environment **113** (Supplement 1): S38–S55.

BUDDENBAUM, H. & STEFFENS, M., 2011: Laboratory imaging spectroscopy of soil profiles. – Journal of Spectral Imaging **2** (a2): 1–5.

BUDDENBAUM, H. & STEFFENS, M., 2012a: The Effects of Spectral Pretreatments on Chemometric Analyses of Soil Profiles Using Laboratory Imaging Spectroscopy. – Applied and Environmental Soil Science **2012:** 12.

BUDDENBAUM, H. & STEFFENS, M., 2012b: Mapping the distribution of chemical properties in soil profiles using laboratory imaging spectroscopy, SVM and PLS regression. – EARSeL eProceedings **11** (1): 25–32.

BUDDENBAUM, H. & HILL, J., 2015: PROSPECT Inversions of Leaf Laboratory Imaging Spectroscopy – a Comparison of Spectral Range and Inversion Technique Influences. – PFG – Photogrammetrie, Fernerkundung, Geoinformation **2015** (3): 231–240.

BUDDENBAUM, H., STERN, O., PASCHMIONKA, B., HASS, E., GATTUNG, T., STOFFELS, J., HILL, J. & WERNER, W., 2015: Using VNIR and SWIR Field Imaging Spectroscopy for Drought Stress Monitoring of Beech Seedlings. – International Journal of Remote Sensing **36** (18): 4590–4605.

FARIFTEH, J., VAN DER MEER, F.D., ATZBERGER, C. & CARRANZA, E.J.M., 2007: Quantitative analysis of salt-affected soil reflectance spectra: A comparison of two adaptive methods (PLSR and ANN). – Remote Sensing of Environment **110:** 59–78.

FARIFTEH, J., van der MEER, F., van der MEIJDE, M. & ATZBERGER, C., 2008: Spectral characteristics of salt-affected soils: A laboratory experiment. – Geoderma **145** (3–4): 196–206.

FRIEDMAN, J. H., 1991: Multivariate Adaptive Regression Splines. – The Annals of Statistics **19** (1): 1–67.

HARTEMINK, A.E. & MINASNY, B., 2014: Towards digital soil morphometrics. – Geoderma **230–231:** 305–317.

HEINZE, S., VOHLAND, M., JOERGENSEN, R. G. & LUDWIG, B., 2013: Usefulness of near-infrared spectroscopy for the prediction of chemical and biological soil properties in different long-term experiments. – Journal of Plant Nutrition and Soil Science **176** (4): 520–528.

JUNG, A., VOHLAND, M. & THIELE-BRUHN, S., 2015: Use of A Portable Camera for Proximal Soil Sensing with Hyperspectral Image Data. – Remote Sensing **7** (9): 11434.

KOKALY, R.F. & CLARK, R.N., 1999: Spectroscopic Determination of Leaf Biochemistry Using Band-Depth Analysis of Absorption Features and Stepwise Multiple Linear Regression. – Remote Sensing of Environment **67** (3): 267–287.

MARABEL, M. & ALVAREZ-TABOADA, F., 2013: Spectroscopic Determination of Aboveground Biomass in Grasslands Using Spectral Transformations, Support Vector Machine and Partial Least Squares Regression. – Sensors **13** (8): 10027–10051.

MULDERS, M.A., 1987: Remote Sensing in Soil Science. – Elsevier Science Publishers B.V., Amsterdam, The Netherlands, ISBN: 978-0-444-42783-0.

NAWAR, S., BUDDENBAUM, H., HILL, J. & KOZAK, J., 2014: Modelling and Mapping of Soil Salinity with Reflectance Spectroscopy and Landsat Data Using Two Quantitative Methods (PLSR and MARS). – Remote Sensing **6** (11): 10813–10834.

NAWAR, S., BUDDENBAUM, H. & HILL, J., 2015: Estimation of soil salinity using three quantitative methods based on visible and near-infrared reflectance spectroscopy: a case study from Egypt. – Arabian Journal of Geosciences **8** (7): 5127–5140.

PEDDLE, D.R., WHITE, H.P., SOFFER, R.J., MILLER, J.R. & LEDREW, E.F., 2001: Reflectance processing of remote sensing spectroradiometer data. – Computers & Geosciences **27** (2): 203–213.

SCHLERF, M., ATZBERGER, C., HILL, J., BUDDENBAUM, H., WERNER, W. & SCHÜLER, G., 2010: Retrieval of chlorophyll and nitrogen in Norway spruce (Picea abies L. Karst.) using imaging spectroscopy. – International Journal of Applied Earth Observation and Geoinformation **12** (1): 17–26.

STEFFENS, M. & BUDDENBAUM, H., 2013: Laboratory imaging spectroscopy of a stagnic luvisol profile – High resolution soil characterisation, classification and mapping of elemental concentrations. – Geoderma **195–196:** 122–132.

STEFFENS, M., KOHLPAINTNER, M. & BUDDENBAUM, H., 2014: Fine spatial resolution mapping of soil organic matter quality in a Histosol profile. – European Journal of Soil Science **65** (6): 827–839.

STENBERG, B., 2010: Effects of soil sample pretreatments and standardised rewetting as interacted with sand classes on Vis-NIR predictions of clay and soil organic carbon. – Geoderma **158** (1–2): 15–22.

STONER, E.R. & BAUMGARDNER, M.F., 1981: Characteristic Variations in Reflectance of Surface Soils. – Soil Science Society of America Journal **45:** 1161–1165.

UDELHOVEN, T., EMMERLING, C. & JARMER, T., 2003: Quantitative analysis of soil chemical properties with diffuse reflectance spectrometry and partial least-square regression: A feasibility study. – Plant and Soil **251:** 319–329.

VISCARRA ROSSEL, R.A., WALVOORT, D.J.J., MCBRATNEY, A.B., JANIK, L.J. & SKJEMSTAD, J.O., 2006: Visible, near infrared, mid infrared or combined diffuse reflectance spectroscopy for simultaneous assessment of various soil properties. – Geoderma **131** (1–2): 59–75.

VISCARRA ROSSEL, R.A., CATTLE, S.R., ORTEGA, A. & FOUAD, Y., 2009: In situ measurements of soil colour, mineral composition and clay content by vis-NIR spectroscopy. – Geoderma **150** (3–4): 253–266.

VISCARRA ROSSEL, R.A. & BEHRENS, T., 2010: Using data mining to model and interpret soil diffuse reflectance spectra. – Geoderma **158** (1–2): 46–54.

VISCARRA ROSSEL, R.A. & WEBSTER, R., 2011: Discrimination of Australian soil horizons and classes from their visible-near infrared spectra. – European Journal of Soil Science **62** (4): 637–647.

VISCARRA ROSSEL, R.A., CHEN, C., GRUNDY, M.J., SEARLE, R., CLIFFORD, D. & CAMPBELL, P.H., 2015: The Australian three-dimensional soil grid: Australia's contribution to the GlobalSoilMap project. – Soil Research, CSIRO Publishing.

VOHLAND, M., BOSSUNG, C. & FRÜND, H.-C., 2009: A spectroscopic approach to assess trace-heavy metal contents in contaminated floodplain soils via spectrally active soil components. – Journal of Plant Nutrition and Soil Science **172** (2): 201–209.

VOHLAND, M. & EMMERLING, C., 2011: Determination of total soil organic C and hot water-extractable C from VIS-NIR soil reflectance with partial least squares regression and spectral feature selection techniques. – European Journal of Soil Science **62** (4): 598–606.

WOLD, S., SJÖSTRÖM, M. & ERIKSSON, L., 2001a: PLS-regression: a basic tool of chemometrics. – Chemometrics and Intelligent Laboratory Systems **58** (2): 109–130.

WOLD, S., TRYGG, J., BERGLUND, A. & ANTTI, H., 2001b: Some recent developments in PLS modeling. – Chemometrics and Intelligent Laboratory Systems **58** (2): 131–150.

WRB, I.W.G., 2014: World Reference Base for Soil Resources 2014. – FAO International soil classification system for naming soils and creating legends for soil maps 106, Rome, Italy.

Addresses of the Authors:

SIMON SCHREINER & Dr. HENNING BUDDENBAUM, University of Trier, Environmental Remote Sensing & Geoinformatics, D-54286 Trier, Germany, Tel.: +49-651-201-4729, e-mail: {s6sischr}{buddenbaum}@uni-trier.de

Prof. Dr. CHRISTOPH EMMERLING, University of Trier, Soil Science, D-54286 Trier, Germany, e-mail: emmerling@uni-trier.de

Dr. MARKUS STEFFENS, Lehrstuhl für Bodenkunde, Department für Ökologie und Ökosystemmanagement, Wissenschaftszentrum Weihenstephan für Ernährung, Landnutzung und Umwelt, Technische Universität München, D-85350 Freising-Weihenstephan, Germany, e-mail: steffens@wzw.tum.de